# Corrosion behaviour of SiC particulate reinforced AZ31 magnesium matrix composite in 3.5% NaCl with and without heat treatment

**Juan Ignacio Ahuir-Torres[1,*], Xinliang Yang[2], Geoff West[3], Hiren R. Kotadia[1,3,**]**

[1]School of Engineering, Liverpool John Moores University, Liverpool L3 3AF, UK

[2]BCAST, Brunel University London, Uxbridge, UB8 3PH, UK

[3]WMG, University of Warwick, Coventry, CV4 7AL, UK

*email: j.i.ahuirtorres@ljmu.ac.uk and **email: h.r.kotadia@ljmu.ac.uk

## Abstract

Magnesium is a lightweight structural material widely utilised in automotive applications. To enhance its mechanical properties, ceramic particulate reinforcement can be incorporated, particularly for wear resistance and high-temperature applications. However, the addition of ceramic particles to magnesium can compromise its corrosion resistance due to microgalvanic cell formation at the interfaces between the Mg matrix and the second phase. This reduces the chemical protection provided by the passive film. In this study, the corrosion properties of AZ31 and AZ31-5SiC samples were investigated, with a focus on the effect of heat treatment. Detailed microstructural and electrochemical analyses revealed that the AZ31 cast sample forms an effective passive film, resulting in improved corrosion resistance. However, the addition of SiC particles to AZ31 increased the corrosion rate, with corrosion mechanisms evolving over time. To mitigate these effects, a heat treatment process was employed to dissolve $\beta$-$Mg_{17}Al_{12}$ eutectic and $Al_8Mn_5$ intermetallic phases. The heat-treated AZ31 with SiC exhibited an improvement in corrosion resistance. These findings highlight the potential for heat treatment to enhance their corrosion resistance, thereby broadening their application prospects.

***Keywords:*** Magnesium AZ31 alloy; Composite Materials; Corrosion; Electrochemical Analyses.

## 1. Introduction

Magnesium alloys are attractive for transportation applications because of their low density (1.738 $g/cm^3$), high specific stiffness, and strength [1]. They also have potential as biodegradable metallic implants because of their good biocompatibility, non-toxicity, and biodegradation properties [2]. Additionally, Mg-alloys have been found to be potential materials for energy storage due to their high gravimetric and volumetric storage capacities [3].

To improve specific strength, creep resistance, thermal shock resistance, and properties at elevated temperatures, composite materials have been developed using Mg as a matrix [4] and reinforced with particles such as silicon carbide (SiC) [5], aluminium oxide ($Al_2O_3$) [6], and titanium carbide (TiC) [7]. The properties of the metal matrix composite (MMC) depend of the type, size, shape, and distribution of the reinforced particles within the Mg matrix [8]. SiC particulate reinforced composite improves wear properties, specifically under lower load and showed superior high temperature properties up to 400 °C [9]. The reinforcement with TiC particles leads to improvements in damping behaviour with yield strength, elastic modulus, and reduced ductility [10]. The addition of $Al_2O_3$ induces good creep resistance and compressive strength due to effective load transfer between the matrix and particles and pinning of the grain boundaries [11]. Carbon nanotube (CNTs) and carbon fibre can also be added to improve the mechanical properties up to 35% [12, 13].

Although addition of an appropriate reinforcement into a Mg-alloy matrix result in improved physical and mechanical properties, these reinforcement particles significantly deteriorate the corrosion properties of the material [14]. Work performed by Hihara and Kondepudi [15, 16] predicted that galvanic corrosion accelerated through SiC particles. Nunez-Lopez et al. [17] determined that pitting or enhanced attack of the matrix due to microgalvanic corrosion in the area of SiC particles. The researcher evaluated the corrosion rate of ZC71 with 12% SiC composite using a salt spray test and concluded that the composite presents a corrosion rate three times higher compared to that of the ZC71 alloy. The formation of less protective corrosion products on the matrix of the composite is the contributing factor to the higher corrosion rate. Zucchi et al. [18] examined the corrosion behaviour of SiC in AZ80A and SiC in ZK60A Mg MMC in sodium sulphate and sodium chloride solutions. Their immersion data and electrochemical test results indicated higher corrosion rates dictated by the composite surfaces, where a stable protective hydroxide film was difficult to form. Chan et al. [19] found that the 20% $Al_2O_3$ in AZ91C Mg MMCs exhibited much more susceptibility to corrosion in chloride-containing solutions compared with the matrix alloy. The corrosion current density ($I_{corr}$) of the composite was approximately equal to that of the matrix alloy in low chloride-concentration

alkaline solutions [20]. When the chloride concentration was increased up to 3.5% NaCl, the $I_{corr}$ of the composite was recorded to be about three times higher than that of the matrix. Xie et al. [21-24] investigated the corrosion resistance of Mg alloys containing rare earth elements in various environments, including saltwater and simulated body fluid. Their findings revealed a significant enhancement in corrosion resistance through heat treatment, leading to microstructural homogenisation. The improvement in corrosion resistance was attributed to the reduction or elimination of microgalvanic cells formed between the Mg matrix and the second phase particles, mitigating the cathodic effect and contributing to increased corrosion resistance. Tiwari et al. [25] observed that the addition of the SiC in the AZ31 Mg alloy reduced the corrosion resistance of Mg matrix. In summary, MMC led to higher corrosion due to the [14]: (i) galvanic coupling of the reinforcement constituent and matrix alloy; (ii) formation of an interfacial phase between the reinforcement and matrix; and (iii) microstructural changes, inhomogeneities and processing contaminants resulted from manufacture of the MMC.

The studies on heat treatments to improve the corrosion resistance of the Mg composite material is limited in the literature. Therefore, the present study was undertaken to understand the relative roles of microgalvanic corrosion and surface film nature on corrosion behaviour of as-cast AZ31 and AZ31 with SiC with heat-treatment condition. Here, this study has used correlative approach bringing together microstructural analysis and electrochemical techniques results. All samples were assessed via several electrochemical techniques (asymmetrical electrochemical noise, potentiodynamic polarisation curve and electrochemical impedance spectroscopy). A detailed microstructural study was performed before and after electrochemical techniques using electron microscopy. The role of $\beta$ - $Mg_{17}Al_{12}$ eutectic, $Al_8Mn_5$ intermetallic (IMC), SiC particles, and influence of the heat treatment on the corrosion mechanism has been carefully considered.

## 2. Experimental procedure

### 2.1 Sample preparation

A commercial AZ31 (Mg-3.29Al-1.02Zn-0.386Mn, in wt. %) Mg-alloy, supplied by Magnesium Elektron Ltd (Manchester, UK). SiC with an average particle size of 4.5 μm supplied by Logitech Ltd (Glasgow, UK). AZ31 sample was melted at 680 °C ($T_{mAZ31}$ ~ 629 °C) under protective gas (95 vol.% $N_2$ + 5 vol.% $SF_6$). SiC particles were pre-heated in an oven at 400 °C for 1 hour to eliminate moisture and prevent chill effects and were added to the AZ31 melt at 680 °C immediately after the pre-heating. **Fig. 1** shown the schematic representation of the synthesis process. The mixing was performed at 680 °C with 5 vol.% SiC particles in two stage (i) mechanical mixing at 650 rpm for 5

min and (ii) intensive shearing at 5,000 rpm for 5 min to achieve high dispersion of the SiC particles [5]. The initial melting process draws the material into the stator, followed by propelling the melt through narrow apertures, achieving high shearing. The shearing process occurred at a temperature of 680 °C, and the composite slurry was shielded by the identical N2 + SF6 gas mixture. AZ31 melt and AZ31-5SiC composite slurry were then cast in a 25 mm diameter cylindrical steel mould. The as-cast ingots were homogenised (heat treated, HT) at 400 °C for 96 h to dissolved $\beta$ - $Mg_{17}Al_{12}$ eutectic phase in Mg matrix and achieve uniform composition throughout the ingot. To calculate the actual volume fraction of SiC in the AZ31 alloy, optical microscopy was performed, and the microstructures processed using ImageJ software. The SiC volume fraction was measured to be 5.54 ± 0.23 % from a total measurement of 20 microstructures covering a 4 $mm^2$ area in AZ31-SiC composite. For simplicity, the composite is named as AZ31-5SiC.

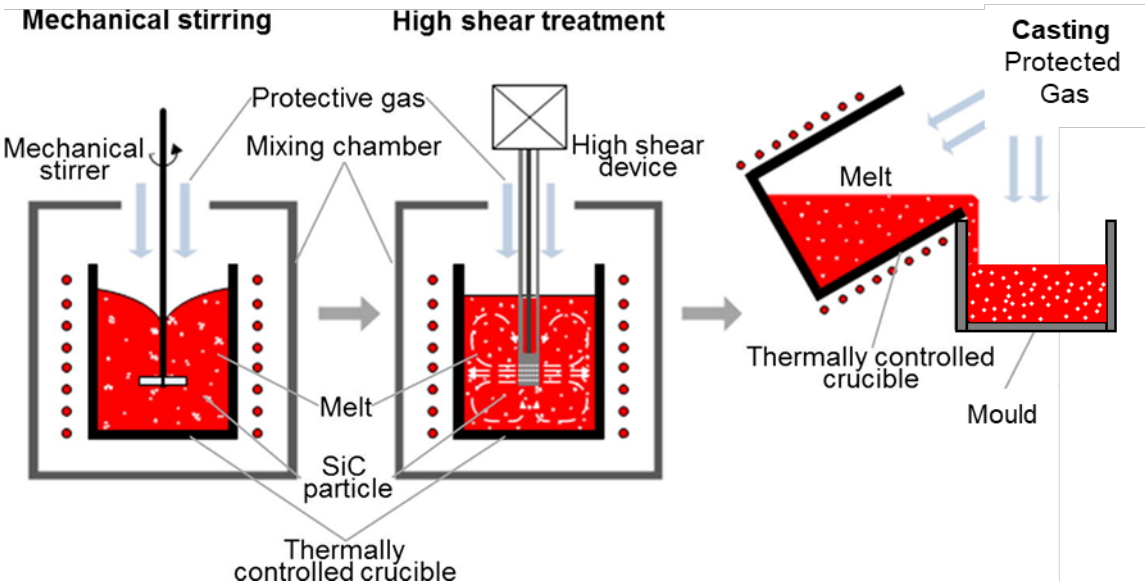


**Fig. 1.** Schematic representation of the synthesis process for SiC particle reinforced AZ31 Mg matrix composite, involving mechanical and high shear treatments before casting to achieve a uniform distribution of SiC particles within the Mg matrix. Note that the figure is not drawn to scale.

### 2.2. Corrosion analysis

The electrochemical analyses were conducted through a potentio/galvanostat (Interface1010E) provided by Gamry Instruments Inc. The potentio/galvanostat was controlled by means of *Gamry Framework* software and the electrochemical data were assessed using *Gamry Echem Analyst* software. All electrochemical assessments were conducted with three-electrode cells. The reference electrode was 3M KCl silver/silver chloride (Ag/AgCl 3M KCl) with double junction from EDT direct ion limited. The counter working electrode consisted of a platinum wire with a diameter of 0.7

mm, supplied by Heimerle + Meule Group. The working electrodes were the samples, each having an exposed area of approximately 0.8 $cm^2$. All corrosion tests were conducted using 40 mL of 0.6M sodium chloride (NaCl) obtained from Merck, and the tests were conducted at room temperature (26 °C). Before corrosion evaluations, the samples were ground with 1200P SiC papers and then polished using 3 μm and then 1 μm polycrystalline diamond paste. A final chemo-mechanical polishing step using colloidal silica was applied. All grit and polishing accessories were supplied by Struers. Before the corrosion study, the samples were cleaned ultrasonically in a bath of ethanol for 5 minutes with subsequent hot air drying.

Three electrochemical assessments were performed: (i) non-perturbative (open circuit potential and zero resistance ammeter), (ii) perturbative of direct current (potentiodynamic polarisation curve, PPC) and (iii) alternating current (electrochemical impedance spectroscopy) [26, 27]. The Open Circuit Potential (OCP) and Zero Resistance Ammeter (ZRA) testing were performed at the same time. The analyses of the potential (OCP) and current density (ZRA) evolution over time were conducted for 2 h with 0.05 seconds of the acquisition time. Electrochemical noise arises from the mixture of these techniques, introducing asymmetry to the system due to the inclusion of the counter electrode. This configuration is referred to as asymmetrical electrochemical noise (AEN) [28].

PPC analysis utilised a cell consisting of a reference electrode, a counter electrode, and a working electrode. The initial potential was -0.3 V (open circuit potential after 2 hours of immersion), with a voltage scan of 0.167 $mVs^{-1}$. The current density limit was set at 0.3 $Acm^{-2}$, and the final potential was 3 V vs the reference electrode potential or at the current density limit. A higher-than-normal current density limit (0.005 $Acm^{-2}$) was chosen due to the elevated current density at low potential (≈1.8V vs reference electrode) observed in the majority of the samples. The potential at open circuit was estimated for two hours of immersion in 0.6 M NaCl.

Electrochemical Impedance Spectroscopies (EIS) were conducted with a 5 mV root mean square potential amplitude, spanning frequencies from 0.01 Hz to 100,000 Hz with 10 points per frequency decade. EIS studies were performed at immersion durations of 2, 24, 48, 72, and 96 hours in 0.6M NaCl to assess the evolution of corrosion mechanisms over time. The equivalent circuit of the EIS data was obtained using ‘Gamry Echem Analyst’ software.

Note that all individual experiments were repeated a minimum of three times, to validate the reproducibility of the data obtained.

**2.3 Material characterisation**

Microstructural analysis was performed before and after PPC corrosion test using a Versa 3D (FEI) Field Emission Gun Scanning Electron Microscope (FEG-SEM), equipped with an Ultim Max 170 (Oxford Instruments) energy-dispersive X-ray spectroscopy (EDX). Images were collected using a BSE (backscattered electron) detector and a nominal current of 8 nA, and a voltage of 20 kV. A Bruker D8 with a Cu tube was used for X-ray Diffraction (XRD) analysis at 40 kV. The spectrum data was Rietveld refined and analysed and by GSAS II crystallography data analysis software [29]. The Vickers hardness tests were performed using a Buehler VH3300 with 50 kgf load and 10 s dwell time. 20 positions were tested for each sample.

## 3. Results and Discussion

### 3.1 Materials analysis

Thermodynamic calculation using Pandat software and Mg database was conducted to understand the phase constitution of the AZ31 in different thermal conditions. The Mg alloy casting process with steel mould produced a high cooling rate (~30 K/s), which is far away from equilibrium solidification. The non-equilibrium Scheil cooling function was used for Thermodynamic calculation. The homogenisation process aimed to produce a uniform chemical distribution within the as-cast AZ31 and AZ31-5SiC composite by diffusion for sufficiently long time. This can be considered as an equilibrium condition. The phase formation under equilibrium condition and Scheil (non-equilibrium) condition is presented in **Fig. 2**. The primary α-Mg phase and $Al_8Mn_5$ IMC are predicted to form in both thermal conditions. The eutectic $\beta$-$Mg_{17}Al_{12}$ is cooling rate sensitive and forms under high cooling rate, where the diffusion may be constrained. To improve readability, when discussing the combined effects of eutectic $\beta$-$Mg_{17}Al_{12}$ and $Al_8Mn_5$ phases, we refer to them as intermetallics (IMCs).

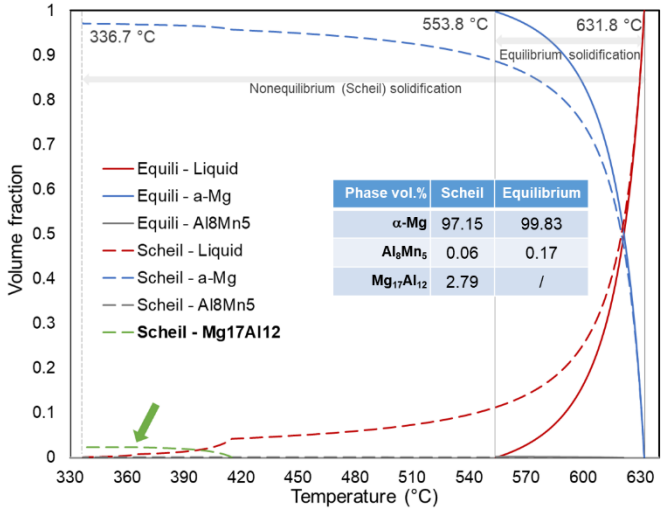

**Fig. 2.** Thermodynamic calculation of the AZ31 alloy phase constitution under different cooling conditions. Scheil cooling condition represents a non-equilibrium solidification where it is towards the casting process that producing the AZ31 and AZ31-5SiC composite ingots. The equilibrium cooling condition here is used to evaluate the phase formation of AZ31 alloy after the homogenisation heat treatment.

**Fig. 3** shows the microstructure of the monolithic AZ31 alloy and AZ31-5SiC composites in the as-cast and HT. It clearly shows that the $\beta$-$Mg_{17}Al_{12}$ phase is in both monolithic alloy and composite in the as-cast condition. After the heat treatment, this divorced eutectic phase has been dissolved into the primary α-Mg phase. The $\beta$-$Mg_{17}Al_{12}$ phase has changed from 0.61 wt.% (as-cast) to 0.09 wt.% (homogenisation) in the monolithic AZ31 alloy using the XRD spectrum calculation with 'Rietveld refinement' (**Fig. 4**).

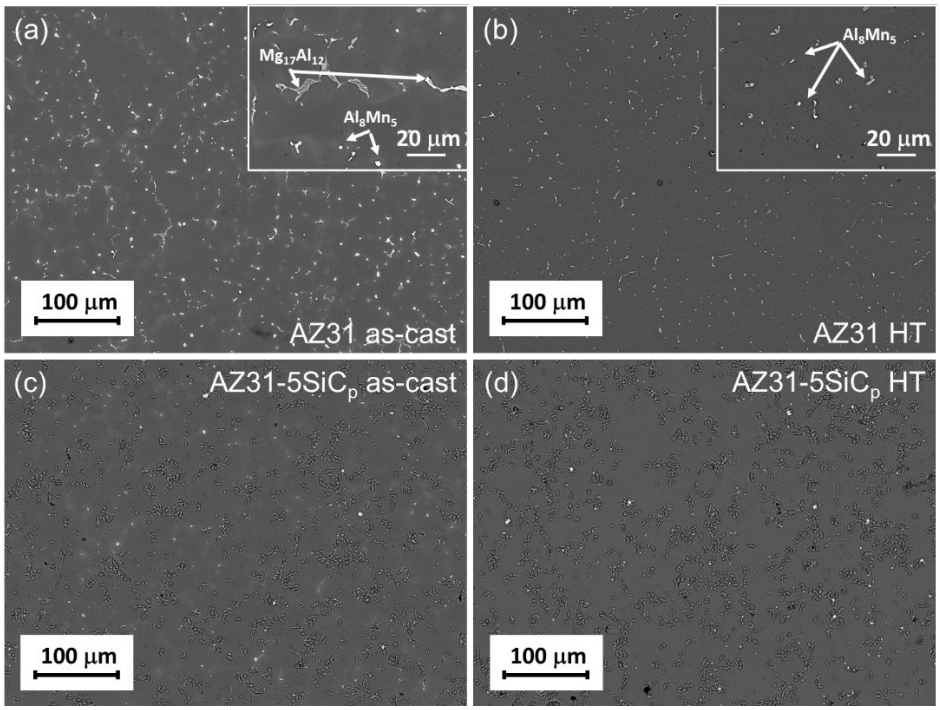


**Fig. 3.** Backscattered electron images of the AZ31 monolithic alloy in (a) as-cast condition, and (b) HT, and AZ31-5SiC composites in (c) as-cast, and (d) HT condition.

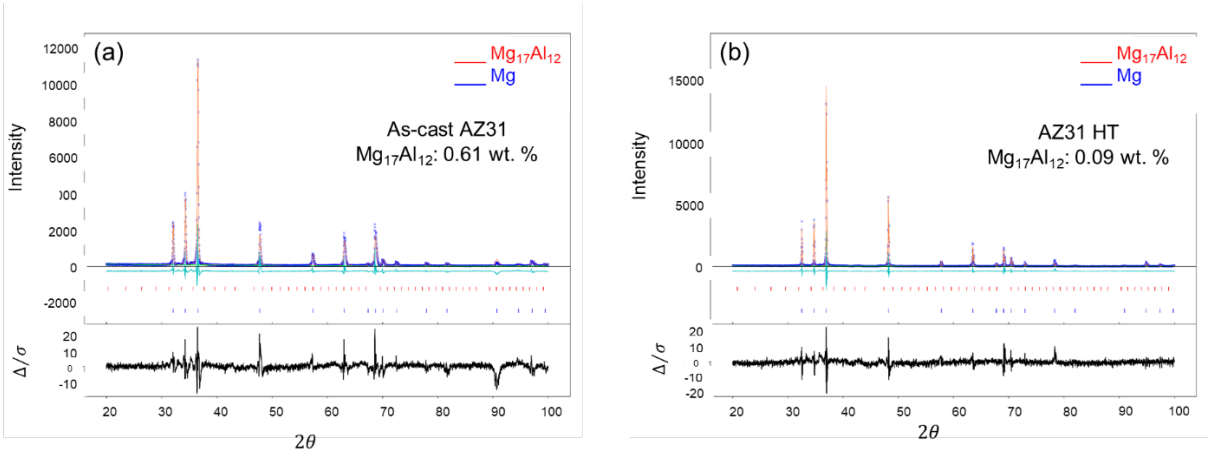


**Fig. 4.** XRD spectra suggested a reduced $\beta$-$Mg_{17}Al_{12}$ phase in the (a) AZ31 as-cast and (b) after the HT.

The Vickers hardness of four samples is shown in **Fig. 5**. There is a decrease of hardness after the homogenisation treatment for both monolithic alloy and MMC. As the hard SiC ceramic particle is present, a significant increase of the hardness can be observed in the composite samples compared to the monolithic alloys. It also indicates a promising wear resistance for the AZ31-5SiC composites.

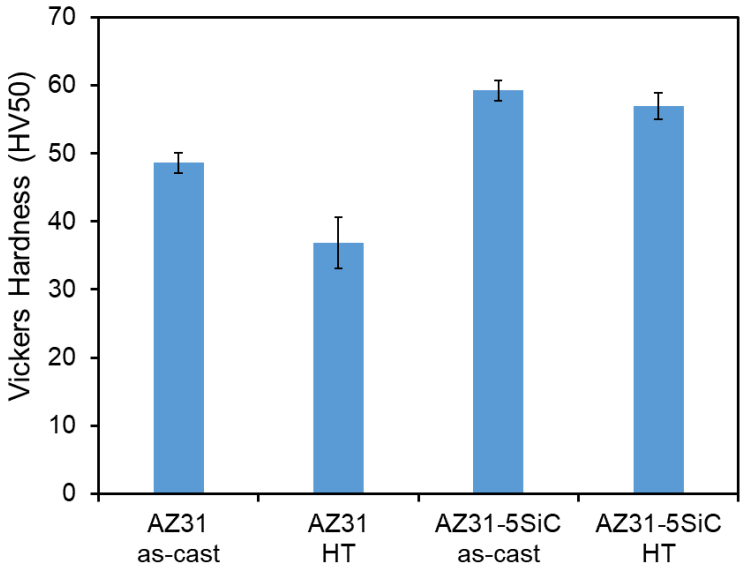


**Fig. 5.** The Vickers hardness of the AZ31 monolithic alloy and AZ31-5SiC composites in as-cast and HT conditions.

### 3.2. Electrochemical Analyses

#### 3.2.1 Open Circuit Potential (OCP) and Zero Resistance Ammeter (ZRA)

**Fig. 6** shows the OCP and ZRA assessments of all samples in 0.6M NaCl dissolution for two hours. Both analysis methods presented fluctuation in their signals over time, indicating the metastable micro-pitting phenomena. When Mg materials are exposed to aggressive environments, the Mg matrix is re-oxidised, resulting in the formation of an oxidised layer of Mg oxide (MgO) and Mg hydroxide ($Mg(OH)_2$) [30, 31]. This layer acts as a barrier to further corrosion, and the increasing potential and reduction of current density are a result of the protective properties of the oxide layer. The presence of the IMCs in Mg matrix can further contribute to fluctuations in the potential and current density over time due to its cathodic effect on the Mg matrix. The Mg surrounding IMCs undergoes dissolution through cathodic effects, leading to their detachment. Within this cavity, the exposed material reacts with water, resulting in the observed increase in current density and a reduction in potential. Subsequently, an oxidised layer reforms on the exposed material, causing a rise in potential and a decrease in current density [31, 32]. A similar effect is observed in AZ31 containing SiC [25].

In **Fig. 6(a)**, the potential of the as-cast AZ31 was shown to oscillate over time around a value of -1.540 V. Meanwhile, in **Fig. 6(b)**, the current density of the material was shown to significantly decrease with time. The oscillations in potential and current density observed in the experiment are due to the deposition/dissolution of corrosion products on the electrode surface, increasing an oxidised layer thickness that increases the corrosion resistance. The increase in potential and decrease in current density observed in the experiment are in accordance with Ohm's law [33]. The dissolution of the magnesium oxide (MgO) layer is driven by the chemical affinity of chloride ions for magnesium cations (Mg). Magnesium chloride ($MgCl_2$) is more thermodynamically stable than magnesium oxide. Consequently, chloride ions react with MgO to form MgCl2, as shown in the following chemical reaction[34-37].

$$MgO_2 + 2Cl^- \rightarrow MgCl_2 + 2O^-$$

The high solubility of $MgCl_2$ in water causes it to dissolve portions of the protective magnesium oxide layer. This dissolution creates imperfections like cracks and pits in the passive film. These imperfections provide the corrosive environment with access to the bare metal surface, leading to an increased corrosion rate. Essentially, chloride anions initiate the corrosion process [34-37]. As a result, the potential is reduced and the current density is increased due to the dissolution process [38]. The fluctuations of as-cast AZ31 observed in the experiment can also be due to the presence of IMXσ, which encourages the dissolution of the oxidised layer [32]. The strong fluctuation in potential and current density observed from 400 s to 3200 s of immersion in 0.6M NaCl indicates that a higher

number of IMCs are being exposed to the aggressive environment, which can increase the frequency of metastable pitting. This results in a substantial region of active exposed material, triggering a prolonged activation-passivation cycle (metastable pitting) when exposed to water and oxygen [30]. The cathodic effect of IMCs, as discussed earlier [31, 32], contributes to this phenomenon. The indication of this corrosion characteristic occurs at specific intervals, primarily due to the presence of non-uniform distribution of IMCs within the matrix. The current density of the as-cast AZ31 material gradually decreases over time until reaching 4000 seconds, indicating an increasing resistance of the oxidised layer [33].

As-cast AZ31-5SiC sample presented stronger fluctuations in potential and current density over time than the as-cast AZ31 material, due to the presence of SiC particles, in addition to the IMCs. These particles possess a cathodic effect on Mg matrix. The fluctuations were found between 2400 s to 4800 s. The total removal of the IMCs on the surface was estimated to be at around 2760 s because the potential remained constant around -1.61 V until 4800 s, while the current density decreased over time (**Fig. 6(a)** and **(b))**. This suggests that the resistance of the oxidised layer increased with time, due to growth of the oxidised layer through corrosion product deposition [33]. The potential (voltage) experiences a decline for immersion durations exceeding 4800 s, while the current density ($Acm^{-2}$) remains constant during this interval, signifying a weakening resistance in the oxidised layer over time. This reduction could be attributed to a decrease in the thickness of the oxidised layer. Consequently, SiC and IMCs contribute to the damage of the passive film, which exhibits spontaneous recovery, leading to fluctuations in both voltage and amperage over time. The non-uniform distribution of particles induces variations in the signals (potential and current density) as the number of particles on the surface undergoes changes throughout the duration.

The potential of the AZ31 with HT generally increased with time, indicating an increase in the oxidised corrosion resistance with time, due to compaction and growth of the oxidised layer [32]. This is opposite to the behaviour of as-cast AZ31 and AZ31-5SiC samples. However, there was a dramatic reduction in potential and increase in current density at 4000 s, which can be caused by the formation of cracks or pits on the oxidised layer, allowing water to access the exposed Mg matrix material. This induces potent microgalvanic corrosion, arising from a small anodic area (cracks and pitting) and a substantial cathodic area (intact passive film), as evidenced by voltage reduction in OCP and ampere increase in ZRA [39]. The formation of these cracks in samples may be attributed to the hydrogen embrittlement process in a neutral environment [40].

The AZ31-5SiC with HT sample showed a rapid increase in potential and quick reduction in current density during the first few seconds of immersion (800 s). This might occur from the formation and increase of the oxidised layer thickness, along with the buildup of corrosion byproducts [32]. After 800 s, the signal (potential and current density) remained constant over time at -1.56 V and 0.005 $Acm^{-2}$, respectively, indicating that the corrosion process is in a dynamic equilibrium. The oxidised layer is created and removed at a consistent frequency, resulting in the protection of its characteristics over time.

In summary, the three samples (as-cast AZ31, AZ31 HT, and AZ31-5SiC HT) had similar potentials (around -1.50 V) as seen in **Fig. 6(a)**, apart from as-cast AZ31-5SiC, which had a lower potential (-1.6 V to -1.65 V). This indicates that the addition of SiC reduces the nobility of the Mg alloy. Nevertheless, HT eliminates or mitigates this effect to a certain extent. AZ31-5SiC HT sample exhibits the lowest current density due to restricted access of aggressive elements to non-corroded material. This limitation reduces from SiC being an oxidised material that cannot undergo further oxidation, as Si is already at its maximum oxidised valence of +4 [41]. The presence of SiC particles on the surface occupied a certain area of the surface, reducing the area available for oxidation, resulting in a lower oxidation rate for the composite compared to the AZ31 over the first two hours of immersion.

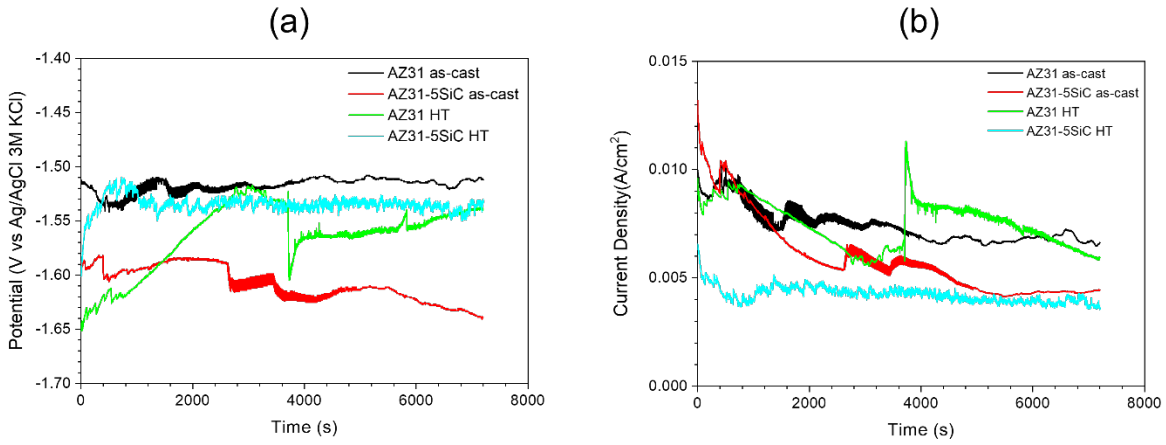


**Fig. 6**. Graphs of the (a) Open Circuit Potential (OCP) and (b) Zero Resistance Ammeter (ZRA) development over time for as-cast and HT samples.

Equations (1) and (2) are used to calculate specific corrosion features from the ZRA and OCP data. **Table 1** contains the results of these calculations, presenting the calculated values of various corrosion features for the spontaneous processes studied.

1. The electrochemical noise corrosion rate ($C.R._{EN}$) of the samples was calculated with the ZRA data and equations (1) [42] and (2) [26].

$$I_{R.M.S} = \sum_{i=N}^{N} \sqrt{\frac{I_i^2}{N}} \quad (1)$$

$$C.R._{EN} = \frac{I_{R.M.S} \times M}{n \times F \times d} \quad (2)$$

Where, $I_{R.M.S.}$ is the current density root mean square, $I_i$ is the current density for each measurement, $N$ is the measurement number, $M$ the Mg molar mass (24.305 g/mol), $n$ is the number of the transferred electrons (2), $F$ is Faraday´s constant (96485 C mol$^{-1}$) and $d$ is the AZ31 alloy density (1.77 g cm$^{-3}$). $C.R._{EN}$ order was following as-cast AZ31≈ AZ31 HT ≈ as-cast AZ31-5SiC > AZ31-5SiC (HT). The $C.R._{EN}$ of all samples was similar to one another, regardless of the HT or the presence of SiC. The results suggest that these factors had insignificant effect on the cathodic corrosion kinetics, or the rate at which the reduction reaction takes place.

2. AEN corrosion resistance ($R_{EN}$) was estimated by means of equation (3) [42], OCP and ZRA data:

$$R_{EN} = \frac{\sigma_E}{\sigma_I} \quad (3)$$

Where, $\sigma_E$ is the standard deviation of the potential values obtained by means of OCP and $\sigma_I$ is the standard deviation of the current density values of the ZRA. The samples that underwent HT had higher $R_{EN}$ values compared to those that did not undergo HT. The HT reduced or dissolved the IMCs in the Mg matrix, which can positively impact the corrosion resistance of the material. The as-cast samples had similar $R_{EN}$ values among themselves. The addition of SiC was also found to have minimal influence on the $R_{EN}$.

These kinetic parameters ($R_{EN}$ and $C.R._{EN}$) are associated with reduction reactions resulting from the asymmetrical testing system [28].

3. The local index ($L.I.$) of the samples was calculated with equation (4) [42] and ZRA data:

$$L.I. = \frac{\sigma_I}{I_{R.M.S}} \quad (4)$$

The $L.I.$ value of the samples showed that all samples had a mixed corrosion mechanism, localised and general (≥1 localised corrosion, < 1 and > 0.05 is mixed localised and general and ≤ 0.05 is general) [42].

**Table 1**. Characteristics of spontaneous corrosion processes in as-cast and HT AZ31 and AZ31-5SiC samples.

| Sample | $\sigma_E$ (mV) | $\sigma_I$ (mA cm$^{-2}$) | $I_{R.M.S.}$ (A cm$^{-2}$) | C.R.$_{EN}$ (mm/Year) | $R_{EN}$ (Ω × cm$^2$) | L.I. |
|---|---|---|---|---|---|---|
| AZ31 as-cast | 6.564 | 0.818 | 0.007 | 17 | 8.02 | 0.11 |
| AZ31-5SiC as-cast | 13.736 | 1.126 | 0.005 | 10 | 12.19 | 0.24 |
| AZ31 HT | 30.408 | 1.073 | 0.008 | 17 | 28.33 | 0.14 |
| AZ31-5SiC HT | 7.714 | 0.356 | 0.004 | 9 | 21.69 | 0.08 |

### 3.2.2 Direct Current Technique: Potentiodynamic Polarisation Curve (PPC)

**Fig. 7** presents the results of the PPC testing in 0.6M NaCl from all samples. PPC provided important information about the kinetic (corrosion velocity and, reduction and oxidation reaction control) and thermodynamic (nobility) of the corrosion process [26, 27, 43]. Three of the samples can be seen to have a similar curve shape (**Fig. 7(a)**). The AZ31 with HT sample meanwhile, has a noticeably different curve shape, indicating that the HT has affected its corrosion behaviour.

The cathodic branches of samples (as-cast AZ31 and AZ31-5SiC and AZ31-5SiC (HT)) had an inclined shape on the PPC curve. This indicates an activation control of the reduction reaction. This is likely due to the presence of IMCs and SiC on the surface of the matrix, acting as sites for water reduction [25, 44]. Reduced area of these particles can hinder the access of water to these reduction sites, resulting in a diffusion impedance [45]. The cathodic or reduction reaction is: $2H_2O + 2e^- \rightarrow 2OH^- + H_2$ [21, 22, 24, 38, 46]. The observation of a horizontal anodic branch on the PPC curve indicates that the anodic reaction is controlled by activation, meaning that the oxidised layer has low corrosion resistance. The presence of IMCs and SiC [46, 47], activate the reactivity of the oxidised layer, leading to a decrease in corrosion resistance. All these particles exhibit a cathodic effect on the α-Mg matrix, forming microgalvanic cells where the particles act as the cathode, and Mg matrix serves as the anode. Subsequently, Mg undergoes corrosion, while particles act as reduction areas. This corrosion results in the dissolution of Mg around the particles, leading to the detachment of IMCs and SiC particles. The detachment induces localised damage to the passive film, promoting internal corrosion of the material. A schematic representation of this mechanism is shown in **Fig. 8**.

The microgalvanic corrosion mechanisms were found to be similar for IMCs and SiC particles, is due to their higher corrosion potential compared to the α-Mg matrix. Notably, the microgalvanic cell is only formed between the α-Mg matrix (anode) and SiC (cathode) in AZ31-5 SiC with HT and can be attributed to the dissolution of IMCs. The chemical reaction at the anodic branch is represented as, $Mg \rightarrow Mg^{+2} + 2e^-$ [21, 23, 38, 46].

The PPC curve of the HT AZ31 sample showed some unique features compared to the other samples. The cathodic branch was inclined, indicating an activation control of the reduction reaction, like the other samples [25, 44]. The slope of the curve was however lower, indicating a stronger activation control. This can be attributed to HT that reduces the IMCs. The activation effect is proportional to particle size [47, 48]. The anodic branch has an irregular shape, with a vertical portion from -1.38 V to -1.46 V, showing the presence of a protective oxidised layer at this potential range. The high current density ($10^{-5}$ A $cm^{-2}$) of this potential range indicates that this layer cannot be considered as a passive film (≈$10^{-6}$ A $cm^{-2}$) [49].

At potentials from -1.46 V to $E_{ul}$ (oxidation layer breaking potential) , the anodic branch showed a horizontal shape, indicating the protective capacity loss of the oxidised layer [22]. The dissolution of the oxidized layer in water exposes the matrix to the harsh environment, leading to the occurrence of pitting corrosion [23, 38]. The hydrogen embrittlement can provoke cracks, causing similar effects [23, 40].

The overall chemical reactions [32, 38, 50]:

$$Mg + 2H_2O \rightarrow Mg(OH)_2 + H_2$$

$$Mg(OH)_2 \leftrightarrow MgO + H_2O$$

Hence, HT distinctly alters the regulation of reduction (from diffusion to activation) and oxidation (from activation to passive) reactions. This modification, however, is limited to HT AZ31, attributed to the absence of SiC and IMCs. In AZ31-5SiC, SiC particles persist after HT, introducing diffusion and activation control for both cathodic and anodic branches in a correlated manner. The same effect is induced by IMCs, and their removal eliminates this influence.

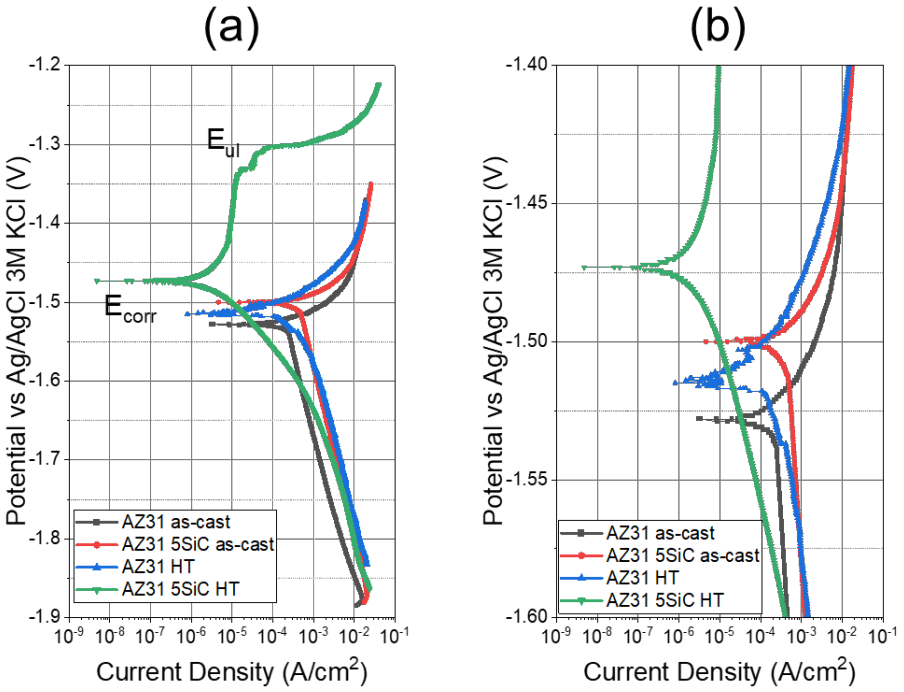


**Fig. 7**. Potentiodynamic Polarization Curves (PPC) for as-cast and HT AZ31 and AZ31 with 5SiC: (a) overall view, and (b) magnified section showing the corrosion potential.

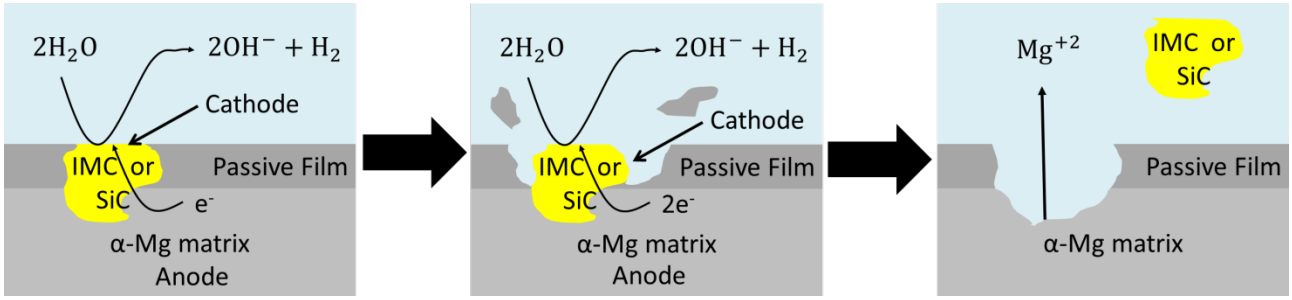


**Fig. 8**. Schematic drawing showing the microgalvanic corrosion mechanism in α-Mg with SiC and IMCs (cathodic effect).

The corrosion rate for PPC ($C.R._{corr}$) is a kinetic factor calculated using equation (3). $C.R._{corr}$ reflects the speed of material oxidation and the overall material deterioration. The $I_{R.M.S.}$ was replaced by corrosion current density ($I_{corr}$) and estimated by the intersection of the cathodic and anodic Tafel lines [51]. The results reveal the order of $C.R._{corr}$: AZ31 HT < AZ31-5SiC HT < as-cast AZ31 < as-cast AZ31-5SiC. The result shows that HT is effective in reducing the corrosion rate ($C.R._{corr}$) in AZ31 and AZ31-5SiC samples. This is likely because the HT leads to homogenisation of the microstructure, which reduces the size and volume fraction of IMCs. It decreases the chemical activation of the IMCs, as mentioned before [25, 44, 48]. The reduction in $C.R._{corr}$ following HT is

more moderate in AZ31-5SiC than in AZ31, primarily because SiC is retained after treatment due to its higher melting point (3100 K [52]) compared to the HT temperature (673 K). However, the dissolution of the IMCs has played a role in enhancing the corrosion resistance of the HT samples. The presence of SiC does not significantly affect the $C.R._{corr}$ of the samples that were not subjected to HT. The cast sample $C.R._{corr}$ was higher than that for HT samples. The larger size and distribution of the IMCs strengthens the cathodic effect that decreases the corrosion resistance of the material, as discussed previously [25, 44, 48]. The comparison of $C.R._{corr}$ and $C.R._{EN}$ of the samples indicate that, in most cases, the actual $C.R._{corr}$ is similar to the estimated $C.R._{EN}$. There is an exception with the HT AZ31 sample, where $C.R._{corr}$ was found to be lower than $C.R._{EN}$. This confirmed that corrosion is controlled by diffusion for almost all samples, with the exception being the HT AZ31 where corrosion is controlled by the protective oxidised layer.

The noble materials have higher corrosion potential ($E_{corr}$) values, indicating a greater thermodynamic stability [25]. The order of $E_{corr}$ is the following: AZ31 HT > AZ31-5SiC HT ≈ as-cast AZ31 ≈ as-cast AZ31-5SiC. The results suggest that most of the samples had similar $E_{corr}$ values. The HT AZ31 sample nevertheless had a higher $E_{corr}$, making it the most noble among the samples. The presence of IMCs, and SiC is believed to decrease the nobility of the samples by activating the Mg matrix [44, 48]. The absence or reduction of these particles in the HT AZ31 sample likely contributed to its increased nobility.

Polarization resistance ($R_p$) is a kinetic characteristic that is used to evaluate the corrosion behaviour of a material. This is inversely proportional to the corrosion velocity. It is calculated with equations (5), (6), and (7) [26].

$$E_{applied} - E_{corr} = \beta_c \times \ln\left(\frac{I}{I_{corr}}\right) \quad (5)$$

$$E_{applied} - E_{corr} = \beta_a \times \ln\left(\frac{I}{I_{corr}}\right) \quad (6)$$

$$R_p = \frac{\beta_a \times \beta_c}{2.303 \times (\beta_a + \beta_c) \times I_{corr}} \quad (7)$$

Where, $I$ is the current density, $E_{applied}$ is the applied potential and $\beta_c$ and $\beta_a$ is the cathodic and anodic slopes, respectively. $R_p$ order was the same as $C.R._{corr}$. The results of the study suggest that the HT AZ31 sample had the highest polarization resistance ($R_p$) among the samples, followed by the HT AZ31-5SiC sample. This is because $R_p$ is proportional to $I_{corr}$. In the case of samples without HT, the values of $R_p$ were similar to the estimated corrosion rate ($R_{EN}$). For the samples with HT, the values

of $R_p$ were higher than $R_{EN}$. This difference could be due to the $R_{EN}$ represents the diffusion impedance of the water, while $R_p$ represents the corrosion resistance that includes this impedance. This suggests that diffusion impedance is reduced with HT. It is notable that $\beta_a$, $\beta_c$, $I_{corr}$, $R_p$ and $C.R._{corr}$ for the cast samples were in coincidence with the work of Tiwari et al [25].

The combination of PPC with equations (2) and from (5) to (7) were employed to evaluating the thermodynamic and kinetic aspects of corrosion behaviour. The calculated thermodynamic factors are summarised in **Table 2**.

**Table 2.** List of the thermodynamic ($E_{corr}$) and kinetic ($\beta_a$, $\beta_c$, $I_{corr}$, $R_p$ and $C.R._{corr}$) PPC corrosion factors of the samples.

| Parameters | Samples | | | |
|---|---|---|---|---|
| | **AZ31 as-cast** | **AZ31-5SiC as-cast** | **AZ31 HT** | **AZ31-5SiC HT** |
| $\beta_a$ (V/decade) | 0.087 | 0.089 | 0.023 | 0.049 |
| $\beta_c$ (V/decade) | -0.149 | -0.136 | -0.027 | -0.066 |
| $I_{corr}$ (mA $cm^{-2}$) | 1.869 | 2.550 | 0.003 | 0.682 |
| $E_{corr}$ (V) | -1.528 | -1.500 | -1.473 | -1.515 |
| $R_p$ ($\Omega \times cm^2$) | 48 | 43 | 18806 | 117 |
| $C.R._{corr}$ (mm/Year) | 41.371 | 56.424 | 0.070 | 15.101 |

### 3.2.3 Alternating Current, Electrochemical Impedance Spectroscopy (EIS)

Nyquist and Bode plots were used to represent the EIS and the equivalent circuit model was used to evaluate the sample corrosion mechanisms. The two different mechanisms could be identified from the impedance spectra and associated with specific features in the Nyquist or Bode plots, as can be seen in **Fig. 9.** The first equivalent circuit comprised of four-time constants used to represent most of the corrosion mechanism. The first time constant can be represented as a resistance and was observed in the Bode plot as a horizontal curve at high frequencies ($10^2$ Hz-$10^5$ Hz) [53]. The second time constant was represented as a combination of a resistance and a capacitor in parallel and was seen as a semi-circle in the Nyquist plots. For the Bode plots, the representation involved an inclined curve for impedance modulus ($Z_{mod}$) as a function of frequency ($F$) and a peak for phase angle ($\theta$) versus frequency ($F$) in both case [53]. The third time constant was also represented with similar elements and in at the same position. This can be observed in the Nyquist plot as a slightly flattened semi-circle, and in the Bode plots as a slope change in the inclined curve ($Z_{mod}$ vs $F$) and as a roundness of the peak ($\theta$ vs $F$). The last time constant was represented as a combination of a resistance and an induction in parallel and was found as a negative loop in the Nyquist plot and an inclined curve with a negative slope in the Bode plot [54].

The minority equivalent circuit was similar to the previous mechanism, but the third time constant was absent. This was observed as roundness of the semi-circle (Nyquist plots), peak sharpness ($Z_{mod}$ vs $F$) and constant slope of the inclined curve ($\theta$ vs $F$). Only the as-cast AZ31-5SiC samples (**Fig. 9(b)** and **Fig. 9(d)**) had a corrosion mechanism presented as this last equivalent circuit, which were at 48 hours, 72 hours and 96 hours of immersion for cast samples and at 2 hours of immersion for HT samples. It is noted that the cause of this dispersion is the adhesion of the chloride ions on the Mg oxide layer [55].

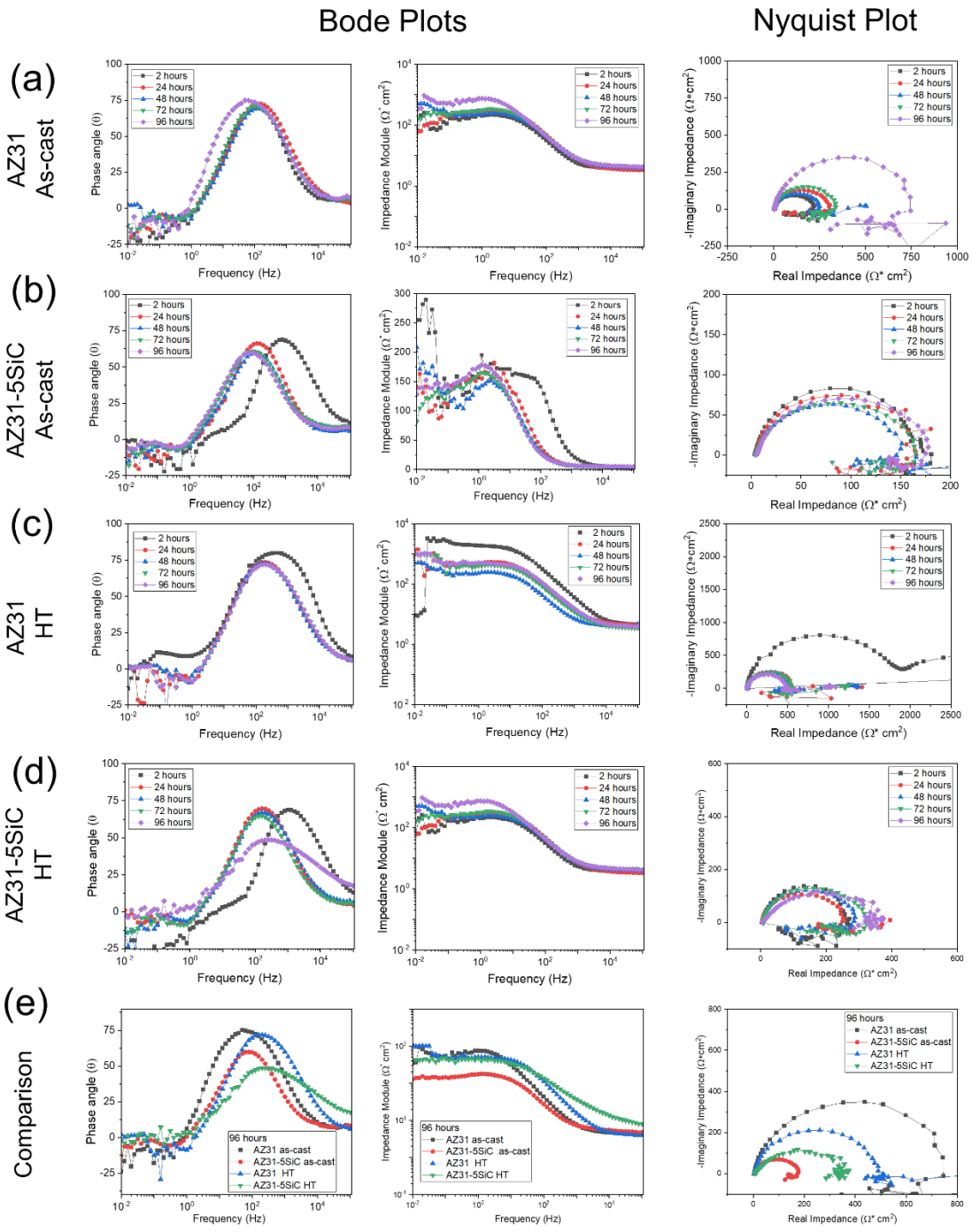

**Fig. 9**. Nyquist and Bode plots of the (a) AZ31 as-cast, (b) AZ31-5SiC as-cast, (c) AZ31 with HT and (d) AZ31-5SiC with HT for 2, 24, 48, 72 and 96 hours in 0.6M NaCl immersion and (e) comparison of the four samples at 96 hours.

**Fig. 10** shows the equivalent circuits proposed to represent the corrosion mechanisms of the samples while **Table 3** lists the values of the circuit equivalent elements. $X^2$ (Chi-square) were from $10^{-3}$ to $10^{-2}$, supporting the validity of the equivalent circuits. The good match between the experimental and simulated data (**Fig. 11**) confirms the validation of the equivalent circuits. The Nyquist and Bode plots at 2 hours and 96 hours of immersion were selected for comparison as they represent more comprehensive data. The simulations showed that the corrosion mechanisms can be represented with the equivalent circuits, being dissimilar according to the sample and immersion time.

The first equivalent circuit, shown in **Fig. 10(a)**, consists of four constant times arranged in a complex circuit configuration. The first element is a resistance ($R_1$) that is in series with the other time constants. The second to third time constants consist of a constant phase element ($CPE_2$ and $CPE_3$) in parallel with a resistance ($R_2$ and $R_3$). $CPE_2$ is in series with $R_2$, while $CPE_3$ and $R_3$ are in parallel with each other. $R_3$ and $CPE_3$ are also in parallel with each other. The last time constant (fourth) of the equivalent circuit are a resistance ($R_4$) in series with an inductor (L), respectively, and they are in parallel with the rest of the circuit elements. It is noted that this equivalent circuit was employed to simulate the AZ31 corrosion mechanism in NaCl [48, 56]. The second equivalent circuit (**Fig. 10(b)**) is similar to the first equivalent circuit, but without the second time constant ($R_2$ and $CPE_2$). This equivalent circuit was used in the literature in saltwater environment [23-25].

The equivalent circuit (EC) was varying according to the immersion time and the sample microstructure (**Table 3)**. These results suggest that the corrosion mechanisms of different samples are complex and can change over time with different immersion conditions. The first equivalent circuit was the majoritarian for all samples and immersion time while the second equivalent circuit was found for some samples with SiC particles (48 hours immersion or more for cast and 2 hours or less immersion for HT). This equivalent circuit was employed in the literature in NaCl environment [23].

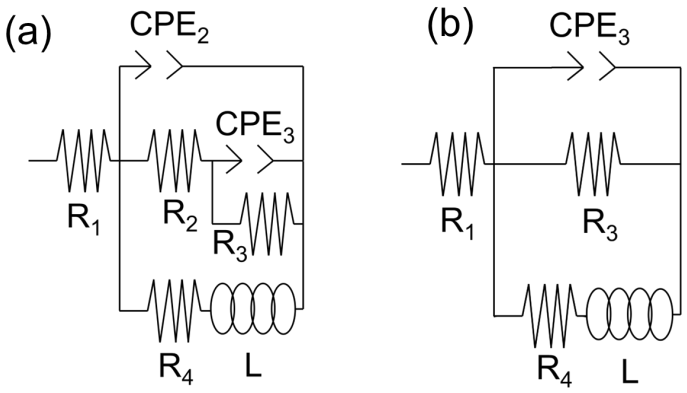


**Fig. 10**. Schematic drawing of (a) first and (b) second equivalent circuit of the corrosion mechanism of the samples in 0.6M NaCl immersion.

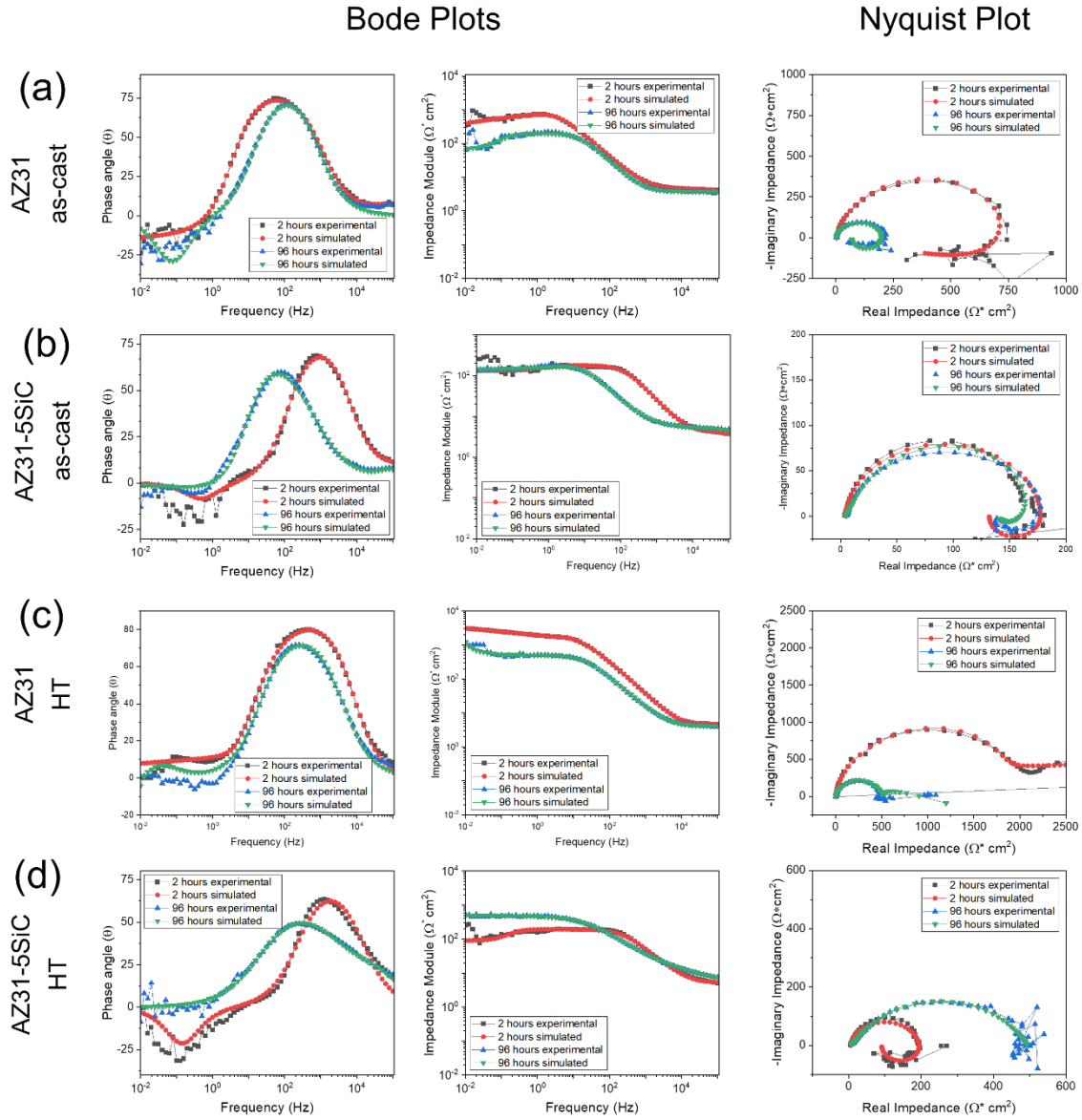

**Fig. 11**. Simulated and real Nyquist and Bode plots of the (a) AZ31 as-cast, (b) AZ31-5SiC as-cast, (c) AZ31 with HT and (d) AZ31-5SiC with HT samples at 2 hours and 96 hours in 0.6M NaCl immersion.

The values of $R_1$ in **Table 3** were found to be similar for all immersion times and samples, which suggests that this resistance can be attributed to the dissolution resistance ($R_s$) to charge movement [47, 48, 50]. The results of the cast materials were similar to [50, 55] and [25] for the samples without and with SiC particles, respectively.

**Table 3.** Corrosion mechanism characteristics obtained using simulation with the simulated equivalent circuit of the Nyquist and Bode plots for the samples at various immersion times.

| Sample | Time (Hours) | $R_1$ ($\Omega \times cm^2$) | $R_2$ ($\Omega \times cm^2$) | $CPE_2$ ($\mu S \times s^n/cm^2$) | $n_2$ | $R_3$ ($\Omega \times cm^2$) | $CPE_3$ ($\mu S \times s^n/cm^2$) | $n_3$ | $R_4$ ($\Omega \times cm^2$) | L ($\Omega \times s/cm^2$) | $X^2$ ($10^{-2}$) |
|---|---|---|---|---|---|---|---|---|---|---|---|
| AZ31 as-cast | 2 | 4.697 | 1453 | 6.89 | 0.93 | 599 | 48.09 | 0.91 | 7838 | 20200 | 0.200 |
| | 24 | 3.514 | 32 | 49.26 | 0.94 | 221 | 830.80 | 0.91 | 221 | 43740 | 2.567 |
| | 48 | 3.972 | 304 | 58.04 | 0.92 | 462 | 1013.00 | 1.00 | 860 | 35220 | 1.826 |
| | 72 | 4.508 | 323 | 60.72 | 0.92 | 2 | 451.80 | 0.92 | 512 | 36270 | 1.160 |
| | 96 | 3.484 | 286 | 61.60 | 0.92 | 3 | 267.70 | 0.88 | 75 | 64820 | 1.007 |
| AZ31-5SiC as-cast | 2 | 4.151 | 2 | 0.28 | 1.00 | 271 | 7.05 | 0.93 | 747 | 7538 | 0.369 |
| | 24 | 6.684 | 196 | 50.26 | 0.93 | 15 | 531.70 | 0.90 | 229 | 43960 | 0.893 |
| | 48 | 4.812 | - | - | - | 182 | 70.60 | 0.92 | 153 | 111400 | 1.388 |
| | 72 | 4.755 | - | - | - | 195 | 50.26 | 0.93 | 296 | 43960 | 2.567 |
| | 96 | 6.083 | - | - | - | 113 | 252.49 | 0.81 | 368 | 9334 | 0.249 |
| AZ31 HT | 2 | 3.884 | 816 | 8.04 | 0.93 | 1403 | 6740.00 | 0.66 | 717 | 25790 | 2.309 |
| | 24 | 4.504 | 10 | 11.45 | 0.96 | 464.40 | 7.71 | 0.97 | 518 | 137600 | 4.795 |
| | 48 | 3.791 | 451 | 37.39 | 0.90 | 13760 | 1915.00 | 1.00 | 838 | 7671 | 4.019 |
| | 72 | 7.995 | 282. | 63.75 | 0.89 | 15520 | 3875.00 | 1.00 | 437 | 163 | 3.243 |
| | 96 | 3.209 | 414 | 32.35 | 0.92 | 1192 | 5991.00 | 1.00 | 916 | 54650 | 1.784 |
| AZ31-5SiC HT | 2 | 4.342 | - | - | - | 148 | 6.27 | 0.94 | 125 | 13550 | 3.454 |
| | 24 | 3.304 | 458 | 42.93 | 0.91 | 1397 | 991.5 | 0.87 | 1218 | 16240 | 0.950 |

| | | | | | | | | | | | |
|---|---|---|---|---|---|---|---|---|---|---|---|
| | 48 | 3.256 | 457 | 41.59 | 0.90 | 5392 | 3370.00 | 1.00 | 759 | 30160 | 2.473 |
| | 72 | 5.116 | 21 | 20.24 | 0.89 | 247 | 35.44 | 0.90 | 442 | 14320 | 0.128 |
| | 96 | 6.021 | 1610 | 0.84 | 0.74 | 1091 | 61.03 | 0.90 | 21140 | 5827000 | 0.296 |

### 3.3 Microstructural analysis after corrosion test

**Fig. 12.** shows that the top and side view of the corroded samples that exhibited $MgO+Mg(OH)_2$ layer. The cast AZ31 samples exhibited a number of cracks and undissolved $\beta$-$Mg_{17}Al_{12}$ eutectic and $Al_8Mn_5$ IMC particles in the oxidised layer. The hydrogen embrittlement is the cause of the crack generation [40] as mentioned previously. The number and size of the cracks were higher in as-cast samples (**Fig. 12(a)** and **(b)**) in comparison to as HT samples (**Fig. 12(c) and (d**)). In addition, $MgO+Mg(OH)_2$ layer is more fragmented and discontinuous in as-cast samples compared with the HT samples. This observation indicates that the HT decreases the imperfections produced during the corrosion process, increasing the corrosion resistance. The generation of imperfections (cracks and pits) is proportional to area fraction of IMCs due to the cathodic effect on Mg matrix [22, 30, 31]. The presence of these cathodic phases also triggers hydrogen embrittlement, resulting in a substantial number of cracks [22, 24]. IMCs size and number are reduced by the HT. In the case of the AZ31 alloys with SiC (**Fig. 12(b)** and **(d)**), the oxidised layer had SiC particles. The high melting temperature of SiC (3100 K [52]) prevents it from dissolving during the HT at 673 K. treatment. These SiC particles are visible in the MgO layer. AZ31 with SiC, HT samples show a continuous oxidised layer in comparison to the AZ31 and AZ31 with SiC cast samples, as shown in **Fig. 12**. It is noted that $Al_8Mn_5$ particles were absent in the corroded samples because of the quick detachment of the particles. The high corrosion potential of these particles produces a great cathodic effect on the matrix, causing the rapid dissolution of the α-Mg matrix around $Al_8Mn_5$. Song and Xun [30] observed that α-Mg matrix dissolved around $Al_8Mn_5$ in only 5 minutes.

Consequently, samples subjected to HT exhibited a reduced occurrence of pits and cracks, attributed to the elimination or reduction of IMCs. This treatment also contributed to the mitigation of oxidised layer dissolution. The cathodic effect of IMCs played a role in generating imperfections and dissolving the oxidised layer, facilitated by their chemical activation and detachment. Chemical activation further promoted hydrogen embrittlement, leading to crack formation. It's noteworthy that the generation of imperfections is influenced by the increase in both the size and number of IMCs [22, 24, 30, 31]. In comparison, AZ31-5SiC with HT exhibited a higher number of imperfections than HT AZ31 due to the constant presence of SiC after treatment. SiC particles had a similar effect on the primary α-Mg matrix as cathodic eutectic and IMC particles. The number of cathodic particles was lower in HT samples than in as-cast samples.

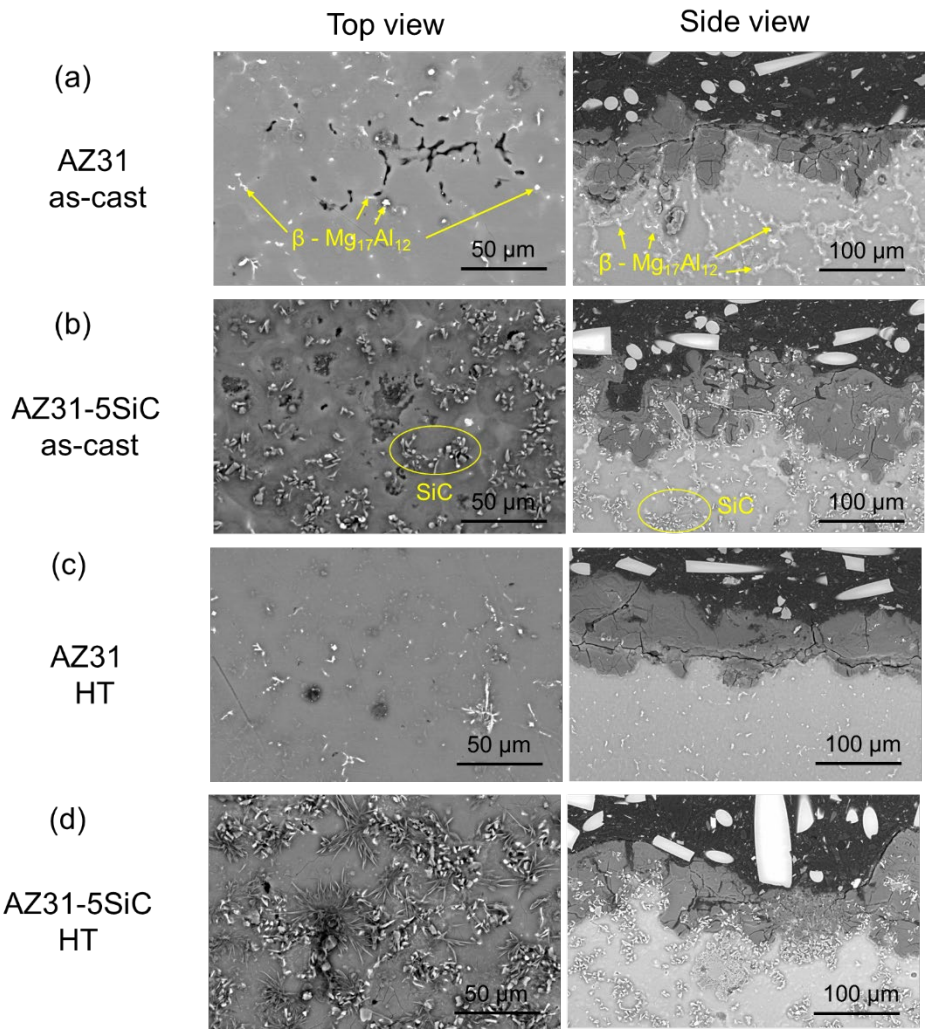


**Fig. 12.** SEM microstructure of the corroded (a) AZ31 as-cast, (b) AZ31-5SiC as-cast, (c) AZ31 as HT, and (d)AZ31-5SiC as HT in top and side view.

## 4. Discussion

By combining the results of electrochemical analysis and Scanning Electron Microscopy (SEM) analyses, this study has provided the following underlying mechanisms of corrosion of all four samples and how they evolve over time using equivalent circuits (**Fig. 13 to 16**).

The equivalent circuit for AZ31 samples varies depending on immersion time of the sample. The second time constant represents the reaction between the oxidised layer on the surface of the samples and the aggressive environment. As can be observed in **Table 3**, the first equivalent circuit was common for all samples at the first hour of immersion. The constant has been named $CPE_2$ or $CPE_{oxi}$, and the resistance in the circuit has been renamed $R_2$ or $R_{oxi}$. Mg alloys are known to naturally generate an oxidised layer when exposed to an aggressive environment [21, 48, 50]. The third time constant in the equivalent circuit

represents the corrosion process of the bare material without its oxidised layer. $R_3$ in the circuit is known as the charge transfer resistance ($R_{ct}$). $CPE_3$ represents the double layer in the interlayer between metal and electrolyte generated by charges alignment ($CPE_{dl}$) [21, 47, 48, 50]. The fourth time constant in the equivalent circuit represents the ion ($Cl^-$) adsorption-desorption process on Mg, where an inductor (L) element is used to model the adsorption process and resistance ($R_4$=$R_{ad\text{-}de}$) is used to model the desorption process [22, 25, 50].

### *4.1 As-cast AZ31*

The first equivalent circuit also had a good correlation with the corrosion mechanism at all immersion times (**Fig. 13**). $CPE_{oxi}$ was increased with time while $R_{oxi}$ was reduced with time. Similar behaviours were observed for $CPE_{dl}$ and $R_{ct}$, correlatively. Both behaviours indicated the continuous degradation and oxidation of the Mg alloy. The high affinity of the chloride ion with Mg oxide deteriorates the protective features of the oxidised film [30, 45, 47, 57]. The generation of hydrogen gas produces cracks on the oxidised film, also diminishing the oxidised layer protection [38, 45]. $CPE_{oxi}$ also increases with time indicating a reduction in the thickness of the oxidised layer. The thickness of the oxidised layer ($d$) is inversely proportional to $CPE_{oxi}$, as indicated by equation (8) [23, 26, 58-61].

$$d = \frac{\varepsilon_o \times \varepsilon}{CPE_{oxi} \times (2 \times \pi \times f)^{n_{oxi}-1}} \quad (8)$$

where, $\varepsilon_o$ is the permittivity of free space, $f$ is the frequency of the phase angle for oxidised layer and $\varepsilon$ is the dielectric constant of oxidised Mg. The continuous dissolution of the oxidised layer with chloride ions continuously decreases the thickness of the oxidised layer [30, 45]. $n_{oxi}$ decreasing over the time indicated the generation of the imperfection (e.g., cracks) on this film. The irregularities on the surface can be represented as a reduction in the value of n [54]. $R_{ad\text{-}de}$ was decreased with the time whilst $L_{ad\text{-}de}$ was enlarged, indicating the promotion of the adhesion processes with the time. The cracks are enlarged with time, producing an increase of the contact area with the dissolution over time. This prompts the adhesion process [38, 45]. It is noted that the deterioration of the material is encouraged with the number and size of the intermetallic and second phase particles [55, 57].

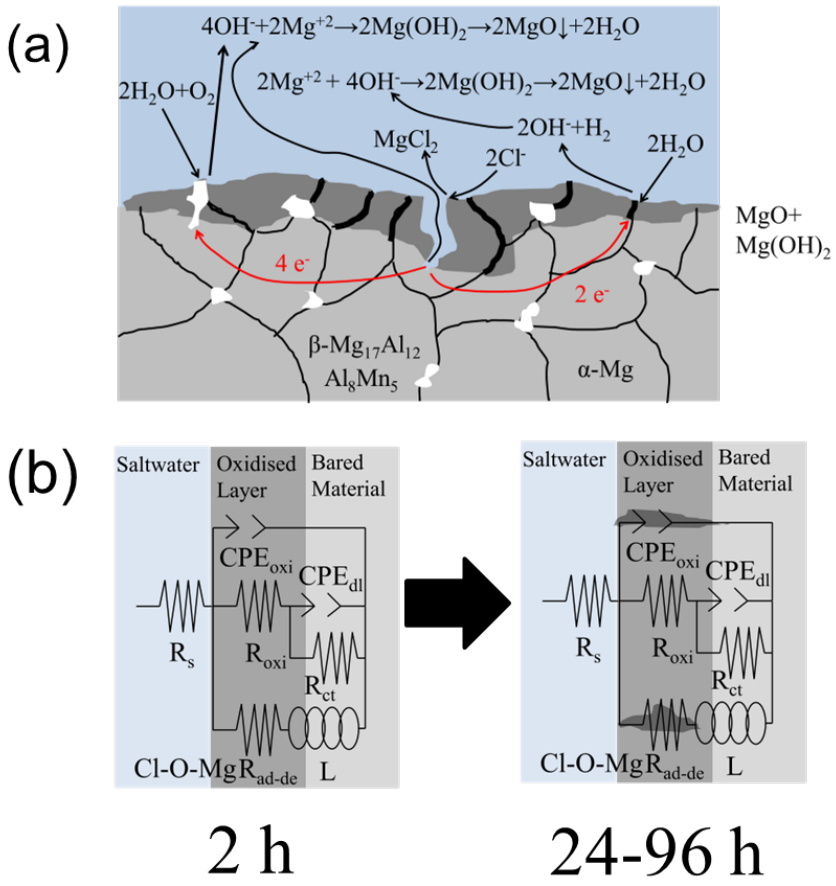


**Fig. 13.** AZ31 sample (a) schematic illustrations of the formation of oxide and chemical reaction, and (b) corrosion mechanism evolution over time using equivalent circuit.

### *4.2 As-cast AZ31-5SiC*

The corrosion mechanism of the AZ31-5SiC samples changed after 24 hours of immersion, as indicated by the results of the EIS test shown in **Fig. 14**. The second equivalent circuit represented the corrosion mechanism for 24 hours of immersion or less while the first equivalent circuit was related with the corrosion mechanism of the samples at 48 hours of immersion or more. This showed that the oxidised layer had a zero protective characteristic after 24 hours due to the high number of imperfections (cracks and pores). The SiC particles [25], and IMCs [32, 56, 62] increase the chemical activity of the oxidised layer, prompting its almost total elimination with the chloride ion reaction. This evolution of the corrosion mechanism with the time was found by Song et al. [55] in simulated body fluid. The low $n_{dl}$ at 96 hours of immersion (0.7) is owing to the dielectric relaxation time [63]. The evolution of the adsorption-desorption time constant elements ($R_{ad\text{-}de}$ and $L_{ad\text{-}de}$) over the time was similar to that for the sample without SiC because the crack evolves with similar behaviour.

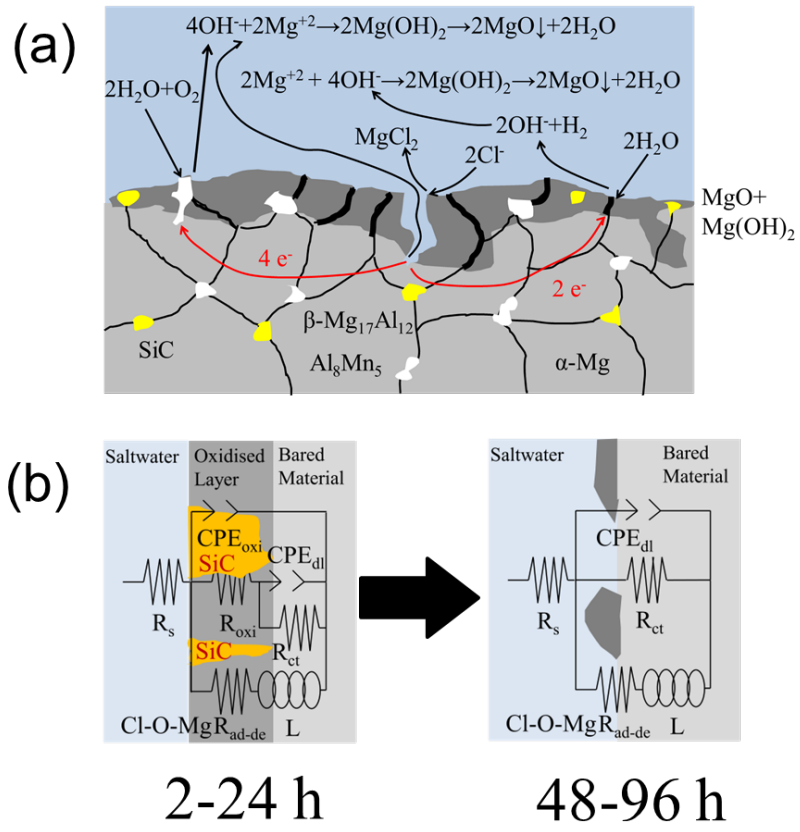


**Fig. 14.** AZ31-5SiC sample (a) schematic illustrations of the formation of oxide and chemical reaction, and (b) corrosion mechanism evolution over time using equivalent circuit.

### *4.3 AZ31after heat treatment*

The EIS data showed that the corrosion mechanism of the AZ31 samples as HT can be represented with the first equivalent circuit for all immersion times (**Fig. 15**). Similar to cast AZ31 samples, $CPE_{oxi}$ and $R_{oxi}$ were increased and reduced with time because of the dissolution of the oxidised layer. Microstructural refinement improves the oxidised layer stability owing to the reduced particle size of the IMCs [30, 31, 48]. $n_{oxi}$ also had similar behaviour to cast AZ31, showing the generation of the imperfection (cracks) with the immersion time. The opposite behaviour was found for $CPE_{dl}$ and $R_{ct,}$ indicating an increment of the chemical inactivity of the exposed material. Thickening of the oxide layer results in quasi-total isolation of the bare material from the aggressive environment [44, 50, 55, 57]. In respect of the adsorption-desorption process, the equivalent circuit elements remained constant with time.

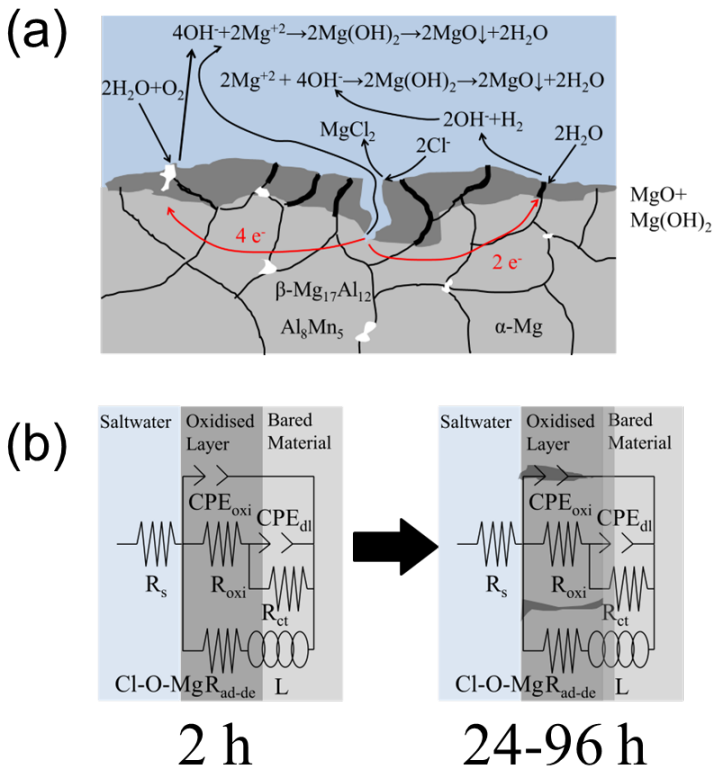


**Fig. 15.** AZ31 sample as HT (a) schematic illustrations of the formation of oxide and chemical reaction, and (b) corrosion mechanism evolution over time using equivalent circuit.

### *4.4 AZ31-5SiC after heat treatment*

The EIS data (**Fig. 16)** for the AZ31-5SiC samples after HT showed an evolution of the corrosion mechanism at 24 hours of immersion and subsequent stabilisation. The second equivalent circuit represented the corrosion mechanism at 2 hours of immersion while the corrosion mechanism for longer immersion time was represented with the first equivalent circuit. This indicates that a semi protective oxidised layer is generated after 24 hours of immersion. SiC particles can encourage the dissolution of the oxidised layer in the first hours of immersion [44, 48]. SiC chemical activation is reduced with time, permitting the formation of an oxidised layer. The reduction of the IMCs effect on oxidation layer due to the HT can also encourages the oxidised layer stability. $CPE_{oxi}$ reduction and $R_{oxi}$ increase with time indicating the thickening of the oxidised layer [64]. This oxidised layer however showed cracks as can be seen in the analyses of the corroded surface (**Fig. 12 (d)**) and the reduction $n_{oxi}$ with the time. The roughness of the surface is inversely proportional to the value of this equivalent circuit element [30-32, 56]. $n_{dl,}$ $CPE_{dl}$ and $R_{ct}$ possessed similar behaviour with time to other samples, showing a possible internal deterioration

with time, as the previous cases. $R_{ad\text{-}de}$ and $L_{ad\text{-}de}$ fluctuated over time, indicating an unstable adsorption-desorption processes over time.

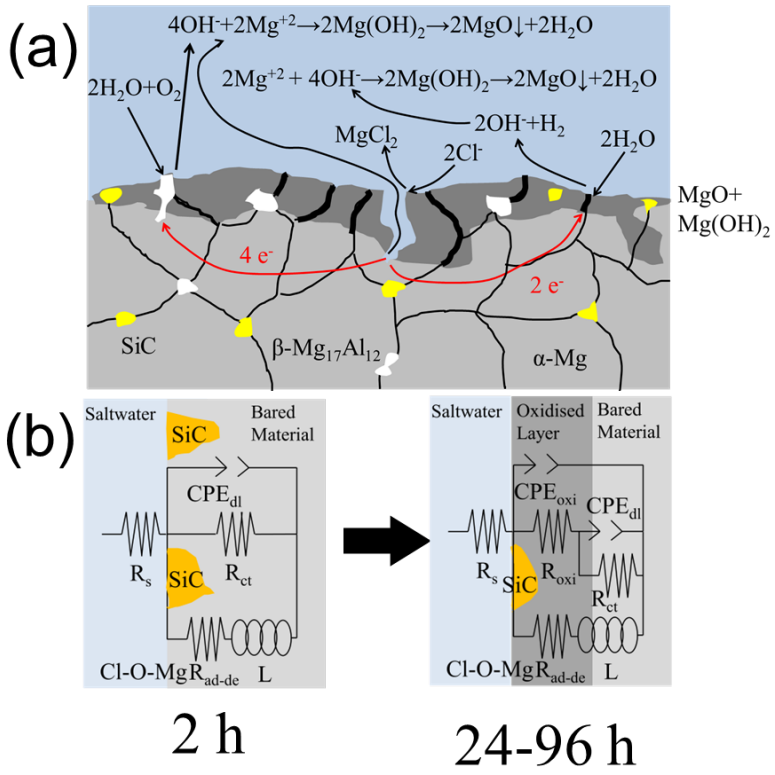


**Fig. 16.** AZ31-5SiC sample as HT (a) schematic illustrations of the formation of oxide and chemical reaction, and (b) corrosion mechanism evolution over time using equivalent circuit.

The dissimilar corrosion mechanism evolution over time of the samples can be attributed to the HT and the presence of SiC particles. The samples with HT showed a more stable oxidised layer than the cast samples due to the reduction in β-phase size, destabilizing the oxidised layer and chemically activating the Mg matrix [21, 30, 31, 44, 48]. The cathodic effects are proportional to the size of these particles [39, 46]. The HT reduced the size of the particles, decreasing the chemical activity of the matrix and oxidised layer. This allows the samples to have an oxidised layer that is less solvable in water. The HT samples with SiC also showed an oxidised layer generated later and with damage (pitting and cracks). The cathodic effect of the SiC on the Mg matrix produced this damage, being stronger than the particle cathodic effect [25, 30, 31]. The SiC particles had good adhesion to the oxidised layer, allowing them to remain in place for longer periods, and produced areas where the adsorption-desorption process occurred. Therefore, the microstructural homogenisation increased the corrosion resistance of the samples due to the elimination or mitigation of the cathodic particles effect on α-Mg matrix.

## 5. Conclusions

This experimental investigation into the corrosion behaviour of AZ31 and AZ31 composite with SiC particles, both with and without heat treatment, through the integration of microstructural and electrochemical analyses. The following conclusion can be drawn from the results:

1. The corrosion resistance of AZ31 alloy and AZ31-5SiC composite is significantly influenced by microstructural features, such as the $\beta$-$Mg_{17}Al_{12}$ eutectic, $Al_8Mn_5$ intermetallic, and SiC particles. This influence is attributed to the development of microgalvanic activities at interfaces between the matrix and second phases, resulting in micro-pitting. However, after heat treatment (homogenisation), these eutectic and intermetallics dissolve into the Mg matrix, reducing microgalvanic activities and enhancing corrosion resistance of the composite sample. This, coupled with the increase in hardness (through SiC), yields a composite material with improved mechanical and chemical properties.

2. Corrosion mechanisms change over time, influenced by variations in sample microstructure. The samples without heat treatment exhibit a decrease in corrosion resistance over time, whereas heat-treated AZ31 shows an increase. Microstructural homogeneity from heat treatment enhances corrosion resistance over time by facilitating the accumulation of oxidation products on the surface. In all samples present mixed (localised and uniform) corrosion. Most samples have an anodic and cathodic branch controlled by diffusion and activation. Heat-treated samples display a cathodic and anodic branch controlled by activation and passivation.

The paper describes the effect of heat treatment on the corrosion behaviour of the composite material and shows that the corrosion resistance can be improved through heat treatment. The resulting composite material has both excellent mechanical properties and improved corrosion resistance.

## Declaration of Competing Interest

The authors have no conflicts of interest.

## Acknowledgement

This work was partially supported by Liverpool John Moore University, Faculty of Engineering and Technology (FET) Pump Prime Awards 2022/23. The authors would like to acknowledge the support provided by the WMG Characterisation Facility partially funded by Higher Education Funding Council for

England (HEFCE) and the WMG Centre High Value Manufacturing Catapult. XLY and HK would like to acknowledge the financial support from EPSRC (EP/W005042/1 and iCASE voucher no. 17000037).

## References

[1] S.V.S. Prasad, S.B. Prasad, K. Verma, R.K. Mishra, V. Kumar, S. Singh, The role and significance of Magnesium in modern day research-A review, Journal of Magnesium and Alloys, 10 (2022) 1-61.
[2] Y. Chen, Z. Xu, C. Smith, J. Sankar, Recent advances on the development of magnesium alloys for biodegradable implants, Acta Biomaterialia, 10 (2014) 4561-4573.
[3] H. Shao, L. He, H. Lin, H.-W. Li, Progress and Trends in Magnesium-Based Materials for Energy-Storage Research: A Review, Energy Technology, 6 (2018) 445-458.
[4] A. Luo, Processing, microstructure, and mechanical behavior of cast magnesium metal matrix composites, Metallurgical and Materials Transactions A, 26 (1995) 2445-2455.
[5] X. Yang, Y. Huang, N.S. Barekar, S. Das, I.C. Stone, Z. Fan, High shear dispersion technology prior to twin roll casting for high performance magnesium/SiCp metal matrix composite strip fabrication, Composites Part A: Applied Science and Manufacturing, 90 (2016) 349-358.
[6] M. Mounib, M. Pavese, C. Badini, W. Lefebvre, H. Dieringa, Reactivity and Microstructure of $Al_2O_3$-Reinforced Magnesium-Matrix Composites, Advances in Materials Science and Engineering, 2014 (2014) 476079.
[7] D.W. Lee, S.V. Aleksandrovkii, V.M. Sizyakov, D.V. Kutsenko, Synthesis of TiC Dispersed Composite in Mg-Alloy Matrix, Magnesium, 2003, pp. 342-347.
[8] A. Mortensen, I. Jin, Solidification processing of metal matrix composites, International Materials Reviews, 37 (1992) 101-128.
[9] S. Jayalakshmi, R. Arvind Singh, S. Mohan, S. Sankaranarayanan, X. Chen, S. Konovalov, M. Gupta, Mechanical Properties and Tribological Behavior of Magnesium Metal Matrix Composites With Micron-Sized and Nano-Sized Reinforcements, in: F.G. Caballero (Ed.) Encyclopedia of Materials: Metals and Alloys, Elsevier, Oxford, 2022, pp. 26-45.
[10] X. Zhang, L. Liao, N. Ma, H. Wang, Mechanical properties and damping capacity of magnesium matrix composites, Composites Part A: Applied Science and Manufacturing, 37 (2006) 2011-2016.
[11] Y.V.R.K. Prasad, K.P. Rao, M. Gupta, Hot workability and deformation mechanisms in Mg/nano–Al2O3 composite, Composites Science and Technology, 69 (2009) 1070-1076.
[12] A.Y. Boroujeni, M. Tehrani, A.J. Nelson, M. Al-Haik, Hybrid carbon nanotube–carbon fiber composites with improved in-plane mechanical properties, Composites Part B: Engineering, 66 (2014) 475-483.
[13] Y. Say, O. Guler, B. Dikici, Carbon nanotube (CNT) reinforced magnesium matrix composites: The effect of CNT ratio on their mechanical properties and corrosion resistance, Materials Science and Engineering: A, 798 (2020) 139636.
[14] F. Khorashadizade, S. Abazari, M. Rajabi, H.R. Bakhsheshi-Rad, A.F. Ismail, S. Sharif, S. Ramakrishna, F. Berto, Overview of magnesium-ceramic composites: mechanical, corrosion and biological properties, Journal of Materials Research and Technology, 15 (2021) 6034-6066.
[15] L.H. Hihara, P.K. Kondepudi, The galvanic corrosion of SiC monofilament/ZE41 Mg metal-matrix composite in 0.5 M NaNO3, Corrosion Science, 34 (1993) 1761-1767,1769.
[16] L.H. Hihara, P.K. Kondepudi, Galvanic corrosion between SiC monofilament and magnesium in NaCl, Na2SO4 and NaNO3 solutions for application to metal-matrix composites, Corrosion Science, 36 (1994) 1585-1595.
[17] C.A. Nunez-Lopez, H. Habazaki, P. Skeldon, G.E. Thompson, H. Karimzadeh, P. Lyon, T.E. Wilks, An investigation of microgalvanic corrosion using a model magnesium-silicon carbide metal matrix composite, Corrosion Science, 38 (1996) 1721-1729.

[18] F. Zucchi, G. Trabanelli, V. Grassi, A. Frignani, Corrosion Behavior in Sodium Sulfate and Sodium Chloride Solutions of SiCp Reinforced Magnesium Alloy Metal Matrix Composites, Corrosion, 60 (2004) 362-368.
[19] W.M. Chan, F.T. Cheng, L.K. Leung, R.J. Horylev, T.M. Yue, Corrosion Behavior Of Magnesium Alloy Az91 And Its Mmc In Nacl Solution, Corrosion97, 1997.
[20] A. Bakkar, V. Neubert, Corrosion characterisation of alumina–magnesium metal matrix composites, Corrosion Science, 49 (2007) 1110-1130.
[21] J. Xie, J. Zhang, Z. Zhang, Z. Yu, Z. Xu, R. Wang, D. Fang, X. Zhang, X. Zhang, R. Wu, Corrosion mechanism of Mg alloys involving elongated long-period stacking ordered phase and intragranular lamellar structure, Journal of Materials Science & Technology, 151 (2023) 190-203.
[22] J. Xie, L. Wang, J. Zhang, L. Lu, Z. Zhang, Y. He, R. Wu, Developing new Mg alloy as potential bone repair material via constructing weak anode nano-lamellar structure, Journal of Magnesium and Alloys, 11 (2023) 154-175.
[23] J. Xie, J. Zhang, Z. Zhang, Q. Yang, K. Guan, Y. He, R. Wang, H. Zhang, X. Qiu, R. Wu, New insights on the different corrosion mechanisms of Mg alloys with solute-enriched stacking faults or long period stacking ordered phase, Corrosion Science, 198 (2022) 110163.
[24] Z. Zhang, J. Xie, J. Zhang, H. Dong, S. Liu, X. Zhang, J. Wang, R. Wu, Simultaneously improving mechanical and anti-corrosion properties of extruded Mg-Al dilute alloy via trace Er addition, Journal of Materials Science & Technology, 150 (2023) 49-64.
[25] S. Tiwari, R. Balasubramaniam, M. Gupta, Corrosion behavior of SiC reinforced magnesium composites, Corrosion Science, 49 (2007) 711-725.
[26] R.G. Kelly, J.R. Scully, D. Shoesmith, R.G. Buchheit, Electrochemical techniques in corrosion science and engineering, CRC Press, 2002.
[27] A.J. Bard, L.R. Faulkner, Fundamentals and applications, Electrochem Methods, 2 (2001) 482.
[28] D.-H. Xia, S. Song, Y. Behnamian, W. Hu, Y.F. Cheng, J.-L. Luo, F. Huet, electrochemical noise applied in corrosion science: Theoretical and mathematical models towards quantitative analysis, Journal of The Electrochemical Society, 167 (2020) 081507.
[29] B. Toby, T. Madden, M. Suchomel, J. Baldwin, R. Von Dreele, A scanning CCD detector for powder diffraction measurements, Journal of Applied Crystallography, 46 (2013) 1058-1063.
[30] G.-L. Song, Z. Xu, Effect of microstructure evolution on corrosion of different crystal surfaces of AZ31 Mg alloy in a chloride containing solution, Corrosion Science, 54 (2012) 97-105.
[31] G.B. Hamu, D. Eliezer, L. Wagner, The relation between severe plastic deformation microstructure and corrosion behavior of AZ31 magnesium alloy, Journal of alloys and compounds, 468 (2009) 222-229.
[32] S. Salman, R. Ichino, M. Okido, A comparative electrochemical study of AZ31 and AZ91 magnesium alloy, International Journal of Corrosion, 2010 (2010).
[33] R. Cottis, The significance of electrochemical noise measurements on asymmetric electrodes, Electrochimica Acta, 52 (2007) 7585-7589.
[34] L. Wang, T. Shinohara, B.-P. Zhang, Influence of chloride, sulfate and bicarbonate anions on the corrosion behavior of AZ31 magnesium alloy, Journal of alloys and compounds, 496 (2010) 500-507.
[35] D.d.G. Jones, H. Masterson, Effect of chloride concentration on the aqueous corrosion of a magnesium alloy, Nature, 191 (1961) 165-166.
[36] R. Ambat, N.N. Aung, W. Zhou, Studies on the influence of chloride ion and pH on the corrosion and electrochemical behaviour of AZ91D magnesium alloy, Journal of Applied Electrochemistry, 30 (2000) 865-874.
[37] H. Altun, S. Sen, Studies on the influence of chloride ion concentration and pH on the corrosion and electrochemical behaviour of AZ63 magnesium alloy, Materials & Design, 25 (2004) 637-643.
[38] S. Abbasi, M. Aliofkhazraei, H. Mojiri, M. Amini, M. Ahmadzadeh, M. Shourgeshty, Corrosion behavior of pure Mg and AZ31 magnesium alloy, Protection of Metals and Physical Chemistry of Surfaces, 53 (2017) 573-578.

[39] Z. Wang, Y. Wang, C. Wang, Area ratio of cathode/anode effect on the galvanic corrosion of high potential difference coupling in seawater, IOP Conference Series: Materials Science and Engineering, IOP Publishing, 2018, pp. 022046.
[40] A. Srinivasan, K.S. Shin, N. Rajendran, Applications of dynamic electrochemical impedance spectroscopy (DEIS) to evaluate protective coatings formed on AZ31 magnesium alloy, RSC advances, 5 (2015) 29589-29593.
[41] G.L. Harris, Properties of silicon carbide, Iet, 1995.
[42] F. Mansfeld, Z. Sun, Localization index obtained from electrochemical noise analysis, Corrosion, 55 (1999) 915-918.
[43] S. Esmailzadeh, M. Aliofkhazraei, H. Sarlak, Interpretation of cyclic potentiodynamic polarization test results for study of corrosion behavior of metals: a review, Protection of metals and physical chemistry of surfaces, 54 (2018) 976-989.
[44] M.G. Acharya, A.N. Shetty, The corrosion behavior of AZ31 alloy in chloride and sulfate media–a comparative study through electrochemical investigations, Journal of Magnesium and Alloys, 7 (2019) 98-112.
[45] B. Jiang, Q. Xiang, A. Atrens, J. Song, F. Pan, Influence of crystallographic texture and grain size on the corrosion behaviour of as-extruded Mg alloy AZ31 sheets, Corrosion Science, 126 (2017) 374-380.
[46] J. Xie, J. Zhang, Z. You, S. Liu, K. Guan, R. Wu, J. Wang, J. Feng, Towards developing Mg alloys with simultaneously improved strength and corrosion resistance via RE alloying, Journal of Magnesium and Alloys, 9 (2021) 41-56.
[47] J. Lei, L. Li, F. Pan, Environmental friendly corrosion inhibitors for magnesium alloys, Magnesium Alloys-Corrosion and Surface Treatments, (2011) 47-64.
[48] H. Chen, J. Tang, W. Gong, Y. Gao, F. Tian, L. Chen, Effects of annealing treatment on the microstructure and corrosion behavior of hot rolled AZ31 Mg alloy, Journal of Materials Research and Technology, 15 (2021) 4800-4812.
[49] M.A. Rodríguez, R.M. Carranza, R.B. Rebak, Passivation and depassivation of alloy 22 in acidic chloride solutions, Journal of The Electrochemical Society, 157 (2009) C1.
[50] S. Tighiouaret, A. Hanna, H. Azzeddine, L. Rabahi, A. Dakhouche, F. Brisset, A.-L. Helbert, T. Baudin, D. Bradai, On the evolution of microstructure, texture and corrosion behavior of a hot-rolled and annealed AZ31 alloy, Materials Chemistry and Physics, 267 (2021) 124598.
[51] K. Kakaei, M.D. Esrafili, A. Ehsani, Graphene and anticorrosive properties, Interface science and technology, Elsevier, 2019, pp. 303-337.
[52] P.S. Sokolov, V.A. Mukhanov, T. Chauveau, V.L. Solozhenko, On melting of silicon carbide under pressure, Journal of Superhard Materials, 34 (2012) 339-341.
[53] D.D. Macdonald, Reflections on the history of electrochemical impedance spectroscopy, Electrochimica Acta, 51 (2006) 1376-1388.
[54] A.J. Bard, L.R. Faulkner, H.S. White, Electrochemical methods: fundamentals and applications, John Wiley & Sons, 2022.
[55] Y. Song, D. Shan, R. Chen, F. Zhang, E.-H. Han, Biodegradable behaviors of AZ31 magnesium alloy in simulated body fluid, Materials Science and Engineering: C, 29 (2009) 1039-1045.
[56] L. Bland, N. Birbilis, J. Scully, Exploring the effects of intermetallic particle size and spacing on the corrosion of Mg-Al alloys using model electrodes, Journal of The Electrochemical Society, 163 (2016) C895.
[57] A. Srinivasan, K.S. Shin, N. Rajendran, Dynamic electrochemical impedance spectroscopy (DEIS) studies of AZ31 magnesium alloy in simulated body fluid solution, Rsc Advances, 4 (2014) 27791-27795.
[58] S. Ghosh, S. Ganguly, A. Maruthi, S. Jana, S. Remanan, P. Das, T.K. Das, S.K. Ghosh, N.C. Das, Micro-computed tomography enhanced cross-linked carboxylated acrylonitrile butadiene rubber with the decoration of new generation conductive carbon black for high strain tolerant electromagnetic wave absorber, Materials Today Communications, 24 (2020) 100989.

[59] S. Ganguly, P. Bhawal, R. Ravindren, N.C. Das, Polymer nanocomposites for electromagnetic interference shielding: a review, Journal of nanoscience and nanotechnology, 18 (2018) 7641-7669.
[60] P. Wang, X. Li, Z. Liu, J. Peng, C. Shi, T. Li, J. Yang, C. Shan, W. Hu, B. Liu, Construction of highly conductive PBI-based alloy membranes by incorporating PIMs with optimized molecular weights for high-temperature proton exchange membrane fuel cells, Journal of Membrane Science, 659 (2022) 120790.
[61] P. Yupapin, Y. Trabelsi, A. Nattappan, S. Boopathi, Performance improvement of wire-cut electrical discharge machining process using cryogenically treated super-conductive state of Monel-K500 alloy, Iranian Journal of Science and Technology, Transactions of Mechanical Engineering, 47 (2023) 267-283.
[62] C. Glover, T. Cain, J. Scully, Performance of Mg-Sn surface alloys for the sacrificial cathodic protection of Mg alloy AZ31B-H24, Corrosion Science, 149 (2019) 195-206.
[63] A. Jimenez-Morales, J. Galvan, R. Rodriguez, J. De Damborenea, Electrochemical study of the corrosion behaviour of copper surfaces modified by nitrogen ion implantation, Journal of Applied Electrochemistry, 27 (1997) 550-557.
[64] Y. Qiao, Y. Zheng, W. Ke, P. Okafor, Electrochemical behaviour of high nitrogen stainless steel in acidic solutions, Corrosion Science, 51 (2009) 979-986.